RESEARCH ARTICLE

Spectral Topography of the Subthalamic Nucleus to Inform Next-Generation Deep Brain Stimulation

Alberto Averna, PhD,[1] Ines Debove, MD,[1] Andreas Nowacki, MD,[2] Katrin Peterman, MSc,[1] Benoit Duchet, PhD,[3,4] Mário Sousa, MD,[1] Elena Bernasconi, MSc,[1] Laura Alva, MD,[1] Martin L. Lachenmayer, MD,[1] Michael Schuepbach, MD,[5] Claudio Pollo, MD,[2] Paul Krack, MD, PhD,[1] Thuy-Anh K. Nguyen, PhD,[2,6] and Gerd Tinkhauser, MD, PhD[1*]

[1]*Department of Neurology, Bern University Hospital and University of Bern, Bern, Switzerland*
[2]*Department of Neurosurgery, Bern University Hospital and University of Bern, Bern, Switzerland*
[3]*Nuffield Department of Clinical Neuroscience, University of Oxford, Oxford, United Kingdom*
[4]*MRC Brain Network Dynamics Unit, University of Oxford, Oxford, United Kingdom*
[5]*Institute of Neurology, Konolfingen, Switzerland*
[6]*ARTORG Center for Biomedical Engineering Research, University of Bern, Bern, Switzerland*

ABSTRACT: Background: The landscape of neurophysiological symptoms and behavioral biomarkers in basal ganglia signals for movement disorders is expanding. The clinical translation of sensing-based deep brain stimulation (DBS) also requires a thorough understanding of the anatomical organization of spectral biomarkers within the subthalamic nucleus (STN).

Objectives: The aims were to systematically investigate the spectral topography, including a wide range of subbands in STN local field potentials (LFP) of Parkinson's disease (PD) patients, and to evaluate its predictive performance for clinical response to DBS.

Methods: STN-LFPs were recorded from 70 PD patients (130 hemispheres) awake and at rest using multicontact DBS electrodes. A comprehensive spatial characterization, including hot spot localization and focality estimation, was performed for multiple sub-bands (delta, theta, alpha, low-beta, high-beta, low-gamma, high-gamma, and fast-gamma (FG) as well as low- and fast high-frequency oscillations [HFO]) and compared to the clinical hot spot for rigidity response to DBS. A spectral biomarker map was established and used to predict the clinical response to DBS.

Results: The STN shows a heterogeneous topographic distribution of different spectral biomarkers, with the strongest segregation in the inferior-superior axis. Relative to the superiorly localized beta hot spot, HFOs (FG, slow HFO) were localized up to 2 mm more inferiorly. Beta oscillations are spatially more spread compared to other sub-bands. Both the spatial proximity of contacts to the beta hot spot and the distance to higher-frequency hot spots were predictive for the best rigidity response to DBS.

Conclusions: The spatial segregation and properties of spectral biomarkers within the DBS target structure can additionally be informative for the implementation of next-generation sensing-based DBS. © 2023 The Authors. *Movement Disorders* published by Wiley Periodicals LLC on behalf of International Parkinson and Movement Disorder Society.

Key Words: adaptive deep brain stimulation; closed-loop deep brain stimulation; local field potentials; subthalamic nucleus; Parkinson's disease; deep brain stimulation programming

***Correspondence to:** Dr. Gerd Tinkhauser, Department of Neurology, Bern University Hospital and University of Bern, Freiburgstrasse, 3010 Bern, Switzerland; E-mail: gerd.tinkhauser@insel.ch

Relevant conflicts of interest/financial disclosures G.T. received financial support from Boston Scientific and Medtronic not related to the present work. Research agreement with RuneLabs is not related to the present work. A.N. received consulting fees from Medtronic not related to this work. M.L.L. received reimbursement for traveling expenses to scientific meetings from Medtronic, Teva Pharmaceutical Industries, Zambon, and BIAL.

Received: 1 November 2022; **Revised:** 13 January 2023; **Accepted:** 27 February 2023

Published online in Wiley Online Library (wileyonlinelibrary.com). DOI: 10.1002/mds.29381

Abbreviations

A	alpha
CE	clinical efficacy
CT	computed tomography
D	delta
DBS	deep brain stimulation
FG	fast-gamma
HB	high-beta
HFO	high-frequency oscillations
HG	high-gamma
LB	low-beta
LFP	local field potentials
LG	low-gamma
MER	microelectrode recording
MNI	Montreal Neurological Institute space
MRI	magnetic resonance imaging
OVL	overlap
PD	Parkinson's disease
PSD	power spectral density
SD	standard deviation
STN	subthalamic nucleus
T	theta

Deep brain stimulation (DBS) is an established therapy for the treatment of advanced stages of movement and neuropsychiatric disorders such as Parkinson's disease (PD).[1] Disadvantages of the state-of-the-art DBS include laborious manual programming procedures as well as the lack of automatic current adjustment to the fluctuating symptom and neurophysiological states.[2] The next generation of DBS could overcome these limitations using brain-sense–guided programming[3-5] and closed-loop adaptive DBS (aDBS).[6,7] The clinical implementation of user-friendly and robust next-generation DBS tools requires a thorough characterization of potential symptom biomarkers.[8] Basal ganglia beta activity is the single best-described symptom biomarker for indexing bradykinesia and rigidity, with a large body of evidence accumulated over the past 20 years.[9-11] However, most movement disorders, for which DBS is used, are characterized by a variety of symptoms, and the landscape of spectral symptom biomarkers is steadily increasing.[8,12,13] The higher-frequency domain such as finely tuned gamma activity has been linked to the occurrence of dyskinesia[14-16] and high-frequency oscillations (HFO) to tremor.[17] HFOs can further be categorized into slow and fast HFO, with slow HFO (SHFO) being more elevated in the *off* medication state compared to fast HFO (FHFO).[18,19] The lower end of the spectrum, including alpha and theta oscillations, has been attributed to non motor symptoms such as impulsivity or emotional processing.[20-22] Spectral features may also show an inverse relationship to symptoms; for example, in contrast to beta oscillations, high power in HFOs is associated with a lower degree of akinesia.[23,24] This bivalent association between spectral markers and symptoms is taking on a relevant role for the optimization of DBS.[4] To better understand the clinical–spectral relationships, the characterization of biomarkers should expand toward the anatomical domain of their distribution within the target structure. It is already well described that beta activity is preferentially located in the dorsolateral motor region of the subthalamic nucleus (STN),[3,25-28] but the spatial metrics and topography of the broad range of spectral biomarkers are not yet fully understood. In this study, we investigated a large data set of PD patients implanted with multicontact DBS leads to characterize and clinically validate the spectral topography of a wide range of frequency bands within the STN for the optimization of next-generation sensing-based DBS.

Patients and Methods

Patients and Surgery

We screened consecutive PD patients who underwent STN DBS surgery at the University Hospital in Bern from December 2015 to December 2021, in whom local field potentials (LFP) were recorded at rest and who signed the general consent (ethics approval, 2017-00551). A total of 70 patients (130 hemispheres) were included after applying these criteria (Fig. S1). The cohort entailed 42 male and 28 female patients, with a mean age of 61.9 $\pm$ 9.5 years at surgery and a mean disease duration of 9.6 $\pm$ 4.5 years. All patients were implanted with the Boston Vercise Cartesia directional leads (Boston Scientific Cartesia, Marlborough, MA). The DBS target was identified on the T2-sequence of the preoperative 3-T magnetic resonance imaging (MRI) and preoperative stereotactic computed tomography (CT) scans (Leksell G frame) using Brainlab Elements software (Brainlab AG, Munich, Germany). Intraoperative targeting was optimized by microelectrode recordings (MER) and selective test stimulation.

LFP Recordings and Signal Processing

Monopolar resting-state LFPs were recorded during awake DBS surgery from all contacts simultaneously for a mean duration of 86 seconds (range: 15–186 seconds) after placing the DBS lead in its final position (see details in Supplementary Material). Dopaminergic medication was withdrawn before surgery (levodopa [L-dopa]: 12 hours, dopamine agonists: 48 hours). LFPs were normalized for each channel separately by subtracting its mean and dividing by the standard deviation (SD) of the 905- to 945-Hz band-pass-filtered signal.[29] The signals were then down-sampled to 800 Hz, high-pass filtered at 0.5 Hz, and notch filtered at 50 Hz and its harmonics (up to 400 Hz). The power spectral density (PSD) was estimated for the following 10 frequency sub-bands:

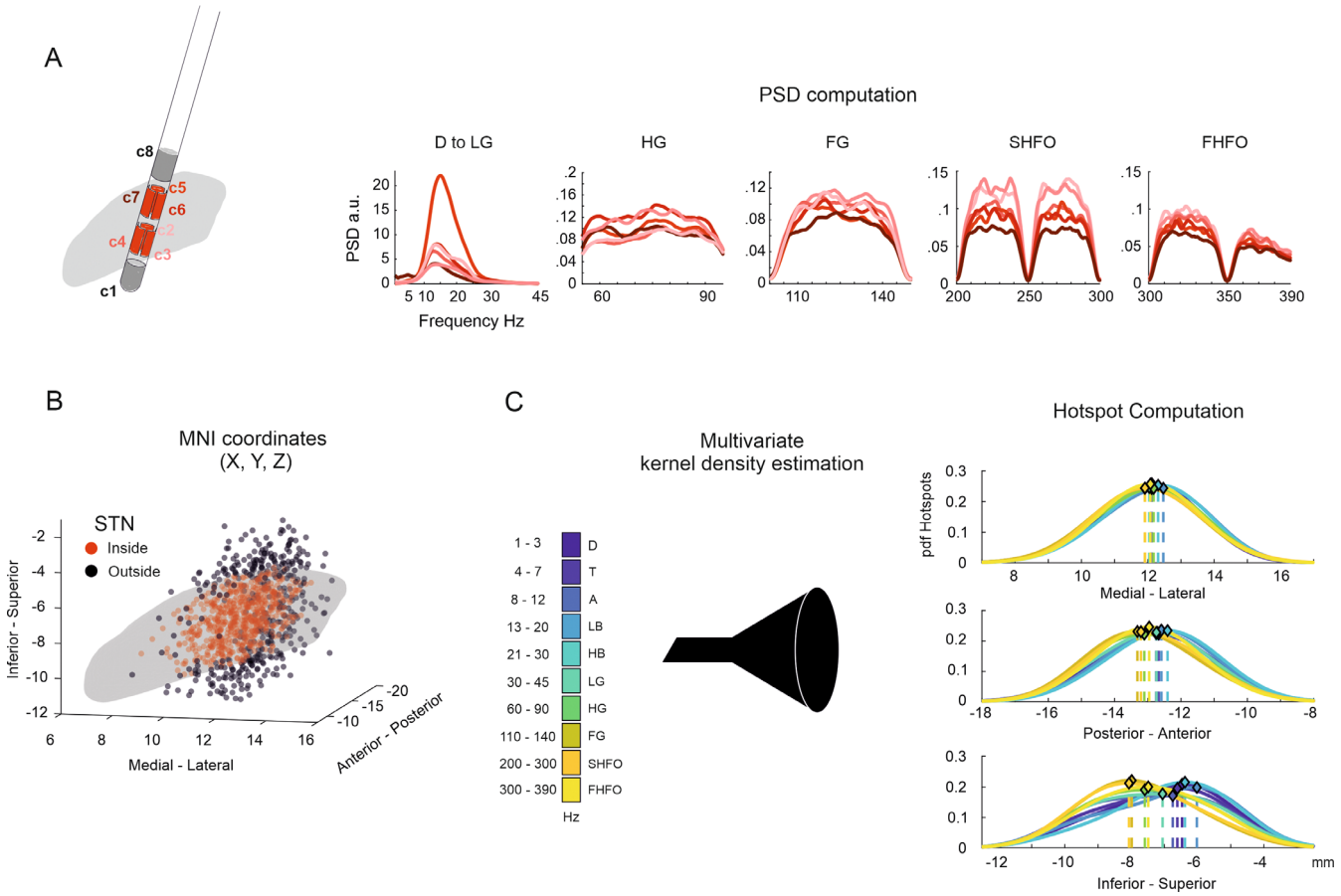

FIG. 1. Computation of the STN spectral topography. (**A**) Schematic illustration of the DBS electrode relative to the STN for an exemplary hemisphere; the contacts localized inside the STN are in red (left). The corresponding power spectra for the contacts inside the STN are reported for different spectral ranges (right): delta- (1–3.5 Hz), theta- (4–7 Hz), alpha- (8–12 Hz), LB- (13–20 Hz), HB- (21–30 Hz), LG- (31–45 Hz), HG- (60–90 Hz), FG- (110–140 Hz), slow high-frequency oscillations (SHFO, 202–298 Hz), and fast high-frequency oscillations (FHFO, 302–390 Hz). (**B**) 3D scatter plot of the contacts of the entire cohort inside (red, n = 611) and outside (black, n = 398) the STN. (**C**) A weighted kernel density estimator was used to compute the spatial probability density distribution (pdf [probability density function]) of the spectral sub-bands across the three anatomical axes (right). The maximum value (dashed lines) corresponds to the center of the spatial hot spot. PSD, power spectral density; DBS, deep brain stimulation; D, delta; T, theta; A, alpha; LB, low-beta; HB, high-beta; LG, low-gamma; HG, high-gamma; FG, fast-gamma; SHFO, slow high-frequency oscillations; FHFO, fast high-frequency oscillations; STN, subthalamic nuclei; MNI, Montreal Neurological Institute space. [Color figure can be viewed at wileyonlinelibrary.com]

delta (1–3.5 Hz), theta (4–7 Hz), alpha (8–12 Hz), low-beta (LB, 13–20 Hz), high-beta (HB, 21–30 Hz), low-gamma (LG, 31–45 Hz), high-gamma (HG, 60–90 Hz), fast-gamma (FG, 110–140 Hz), SHFO (202–298 Hz), and FHFO (302–390 Hz) (Fig. 1A). To further increase the comparability across hemispheres, the PSD of a given spectral feature was normalized over the mean PSD of the same features across all contacts of a given DBS lead. In a further subanalysis, we computed the anatomical hot spot of the single frequency (±2.5 Hz) with maximum power in the beta-frequency band, separately for each hemisphere. This was then compared to the location of the LB and HB hot spots.

Localization of DBS Contacts

The postoperative localization of DBS contacts was performed using the Lead-DBS toolbox in MATLAB.[30] Preoperative MRI and postoperative CT scans were coregistered and normalized to the Montreal Neurological Institute (MNI) space (MNI152 NLIN 2009b).[31] Contacts from both hemispheres were projected onto the right STN (DISTAL atlas[32]) using a nonlinear flip function (further details in Supplementary Material). We also quantified the potential deviations from the surgically intended lead orientation. This showed an average deviation of 26.96° from the surgically intended orientation without preferential direction, which is in the range of previous reports.[33] The detailed approach and results are presented in the Supplementary Material.

Postoperative Clinical Assessment

Patients underwent a monopolar contact review conducted by specialized DBS staff blinded to LFPs, and

this took place on average 5 months (range: 3–10 months) after surgery. The clinical assessment was focused on upper-limb rigidity testing in the *off* medication state (>12 hours of L-dopa and >48 hours of dopamine agonist withdrawal), as this clinical sign is considered the most sensitive for indexing the DBS response during the monopolar contact review.[34] The effect threshold, that is, current necessary to completely relieve rigidity or to obtain the best-achievable improvement, was determined by increasing the amplitude in 0.5-mA steps, whereas the stimulation frequency and pulse width were kept constant at 130 Hz and 60 μs. The "clinical efficacy" (CE) was then defined by the following equation[3,4]:

$$\text{Clinical efficacy (CE)} = \frac{100 \times (\text{rigidity at baseline} - \text{rigidity at effect threshold})}{\text{rigidity at baseline} \times \text{current at effect threshold}}$$

Localization of Spectral Hot Spots and Focality Calculation

To determine the spectral topography of the STN, we considered only contacts localized inside the normalized STN (605 of 1009 contacts) and, furthermore, only hemispheres with at least two contacts inside the STN (n = 115 hemispheres, 68 patients) (Fig. 1). For each DBS lead we then selected the contact with the highest power for each sub-band (Fig. 1A). Using the coordinates and weighted power of these contacts, we computed a multivariate kernel density estimation (kde) of the position of maximum power for each sub-band.[35] The hot spot center position for each frequency band in each axis was defined as the maximum value of the probability density function (pdf) distribution (Fig. 1C). For focality computation we first grouped again the contacts with the highest power for each sub-band and DBS lead. Then we calculated the variance of the distances of this contact pool and compared this to the variance of distances of the total group of contacts inside STN.

Overlap of Clinical and Spectral Hot Spots

The clinical hot spot, indicative of the DBS response, was computed using the CE following the same methodological steps as presented earlier for the spectral hot spots. The following criteria were applied in addition: only hemispheres with at least one point in MDS-UPDRS-III (Movement Disorder Society-Sponsored Revision of the Unified Parkinson's Disease Rating Scale, Part III) upper-limb rigidity at baseline were included (n = 86 hemispheres, ie, 92%, see Fig. S1).

If more than one contact per DBS lead shared the same level of CE, their mean anatomical position was used as input for the clinical hot spot calculation. Results were also generated for using a minimum of two-point rigidity at baseline. To compute the amount of overlap (OVL) between the different spectral hot spots and the clinical hot spot, we first modeled the STN volume as 60 × 60 × 60 3D grid (total: 53,100 grid points). Second, we modeled the spectral and clinical hot spots as 3D ellipsoids, based on the center of their hot spot and the axis lengths defined as the mean absolute distance between the hot spot and all the coordinates generated by the kde. The shared STN volume (grid points) between the spectral and clinical hot spots was then quantified.

Spatial Metrics to Predict the Clinical Response to DBS

To evaluate the predictive value of the spectral topographic map for the clinical response to DBS, we implemented a two-step contact prediction pipeline (see Fig. 5A). The cohort of hemispheres was randomly separated into a training data set (66.7%, 57 of 86 hemispheres) and a test data set (33.3%, 28 of 86 hemispheres). The feature set (predictors) corresponded to the normalized (z scored) Euclidean distance of the stimulation contacts to the center of the anatomical hot spots of the 10 sub-bands. The outcome of the prediction was the normalized (z scored) CE. In the first step, we determined the predictive weights (ie, standardized correlation coefficients) of the feature set. For this, we opted to use an elastic net regression[36] with a fivefold cross-validation in the training data set (see Supplementary Material for further details). The predictive weights reflect the amount and direction of the relationship between the features set (predictors) and the CE and are expressed by the model in a standardized scale, as the input to the model was normalized (z scored). In the second step of this prediction pipeline, we applied the output from step 1 (predictive weights of the feature set) on the test data set to predict the clinical response (CE) to DBS. We then derived the predicted clinical response for the four best features. To increase the generalizability of this prediction method, the entire pipeline was repeated for 1000 iterations, with random allocation of patients to the test and training data sets. In parallel, for each iteration, we also computed the contact prediction expected by chance by shuffling the contact-related predictors for each hemisphere before applying the same two-step prediction pipeline.

Statistical Analyses

Statistical analyses were performed using MATLAB (2020b; Mathworks, Natick, MA). To determine whether the spectral hot spot locations were different from a random distribution, we compared them to

critical values corresponding to the 5% significance level (2-tailed) of the surrogate distributions (1000 surrogate distributions of coordinates, n = 115 contacts each). The distances between all different pairwise combinations of hot spots were tested against the null distribution of differences obtained from the random surrogate distributions. *P*-values were corrected using the Benjamini–Hochberg procedure. To statistically characterize the focality of the sub-band to the total group, we performed a two-sample F-test for equal variances. A repeated-measures analysis of variance was used to test the predicted CE across the four best features, whereas a paired-sample *t*-test was used for single comparison against the outcome of the random prediction. *P*-values from the focality and clinical prediction tests were corrected for multiple comparisons using Bonferroni correction.

Results

Heterogeneous Spatial Distribution of Spectral Hot Spots

A main aim of this work was to determine if and to what degree a set of spectral features, ranging from the delta band through HFO, are spatially segregated within the STN in PD (Fig. 1B). To compute the spectral hot spot distribution, we selected separately for each sub-band the single contact inside the STN with the highest power. Figure 2 shows the spatial distribution of the spectral hot spots across the *x* (ie, medial–lateral), *y* (ie, posterior–anterior), and *z* (ie, inferior–superior) axes and the comparison against a surrogate distribution and between themselves. This revealed a spatial segregation of the spectral hot spots, which is most evident in the inferior–superior axis. More

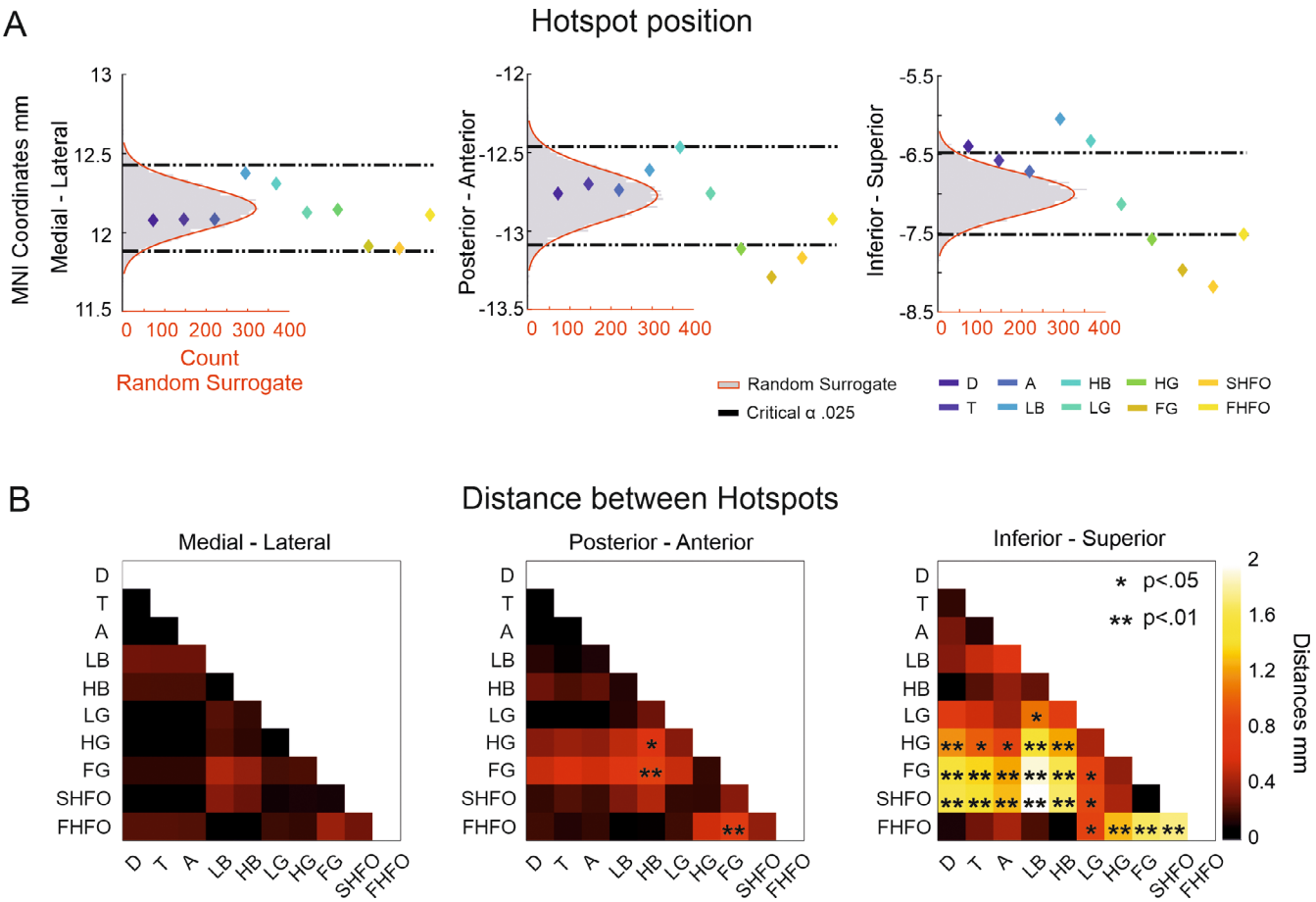

FIG. 2. Spatial distribution of spectral hot spots. (**A**) Top, spectral distribution of spectral sub-bands within the three anatomical axes and relative to the random surrogate distributions (dotted lines; critical values α = [0.025, 0.975], gray bars; histograms of the random surrogate distributions). A spatial segregation of the spectral hot spots from the random distribution is evident in both the inferior–superior and posterior–anterior axes. LB and HB hot spots are localized more superiorly, whereas FG and SHFO are localized more inferiorly relative to the random surrogate distribution. HG and FG hot spots are localized more posteriorly. (**B**) The absolute distance (mm) between the position of all the spectral hot spots within the three anatomical axes (*$P < 0.05$, **$P < 0.01$, after false discovery rate correction). The maximum and significant center-to-center distance in the medial–lateral axis was found between the LB and FG hot spots, in the posterior-anterior axis between HB and FG and in the inferior–superior axis between LB and SHFO. D, delta; T, theta; A, alpha; LB, low-beta; HB, high-beta; LG, low-gamma; HG, high-gamma; FG, fast-gamma; SHFO, slow high-frequency oscillation; FHFO, fast high-frequency oscillation; NS, nonsignificant. [Color figure can be viewed at wileyonlinelibrary.com]

specifically, the spatial hot spots of HG, FG, and SHFO are localized more inferiorly compared to the LB and HB hot spots. This segregation reaches a maximum distance of 1.98 mm ($P < 0.001$) between the centers of the LB and SHFO hot spot. In the posterior-anterior axis we found the HG, FG, and SHFO hot spots localized more posterior in comparison to the random distribution. The largest segregation in the posterior-anterior axis was between the HB and FG hot spots with a center-to-center distance of 0.83 mm ($P < 0.001$). In the medial–lateral axis no spectral hot spot was significantly differently distributed compared to the random distribution. Nevertheless, the within-hot spot segregation revealed a maximum center-to-center distance between the LB and FG hot spots of 0.46 mm (ns), with the LB hot spot being localized more laterally. To confirm that the topographic distribution is not simply a consequence of signal processing and normalization, we replicated the pipeline without any prior normalization of the signals, which provided similar results (Fig. S2). Even if computing the spectral topography using the entire cohort of contacts, thus including contacts localized outside the STN, the relative spectral hot spot distribution is preserved, with only one hot spot (alpha band) falling slightly outside the inferior border of the normalized STN (Fig. S4). Separately we computed the hot spot of the individual maximum beta-power hot spot, which localizes more lateral than the random distribution but remains comparable to the LB and the HB hot spots (Fig. S2).

Hot spot Focality within the STN

After localizing the spectral hot spots within the STN, we further investigated how spatially circumscribed they are. We found that the focality is not only frequency specific but also dependent on the anatomical axes (Fig. 3A). In the following we report on the sub-bands that are spatially more circumscribed (more focal) than the total group of contacts localized within the STN. In the medial–lateral axis, the distributions in the delta (0.75 variance [mm^2]), theta (0.74), alpha (0.77), HB (0.77), LG (0.81), and FHFOs (0.82) are more focal compared to the total group (0.85). In the posterior–anterior axis only the distribution of the FHFO (0.95) sub-band is more circumscribed than the total group (1.05), whereas in the inferior–superior

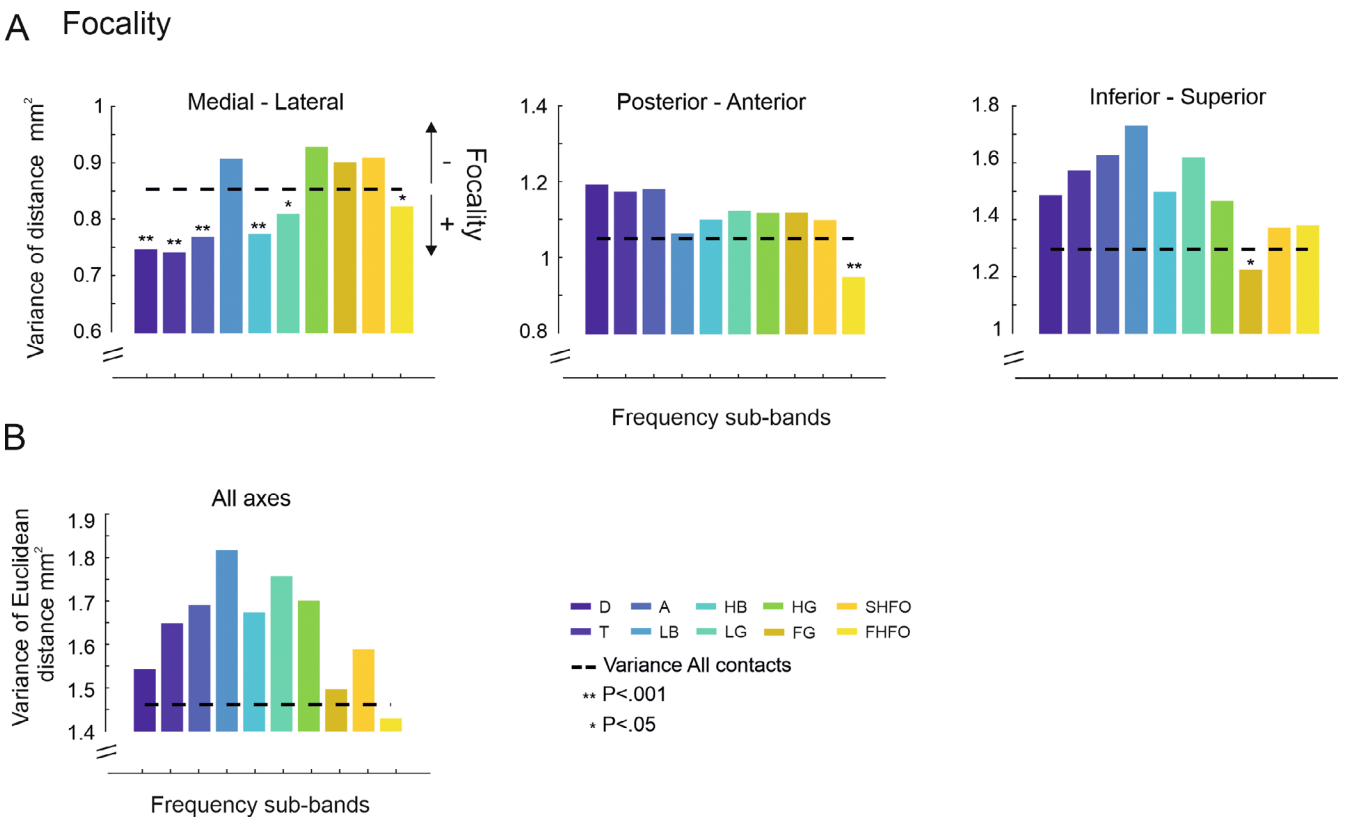

FIG. 3. Spatial focality. (**A**) Spatial extent (focality) of the hot spots across the three specific axes. The dotted line represents the level of variance in the total group of contacts inside the STN (subthalamic nucleus). Delta, theta, alpha, HB, LG, and FHFO are more focal compared to the total group in the medial–lateral axis. In the posterior–anterior axis only FHFO is more focal than the total group. FG is more focal in the inferior–superior axis. (**B**) Color bars showing the level of focality for the Euclidean distances (composite of all axes) for the 10 sub-bands. LB shows the most spread distribution compared to all the other sub-bands, whereas FHFO shows the most circumscribed activity (*$P < 0.05$, **$P < 0.001$); D, delta; T, theta; A, alpha; LB, low-beta; HB, high-beta; LG, low-gamma; HG, high-gamma; FG, fast-gamma; SHFO, slow high-frequency oscillation; FHFO, fast high frequency oscillations. [Color figure can be viewed at wileyonlinelibrary.com]

axis only the FG distribution (1.22) is more focal compared to the total group (1.30). Finally, considering the Euclidean distance as a composite measure for all three axes, none of the spectral feature is more focal than the total group, but the low beta-activity distribution shows the widest spread (1.81), whereas FHFO

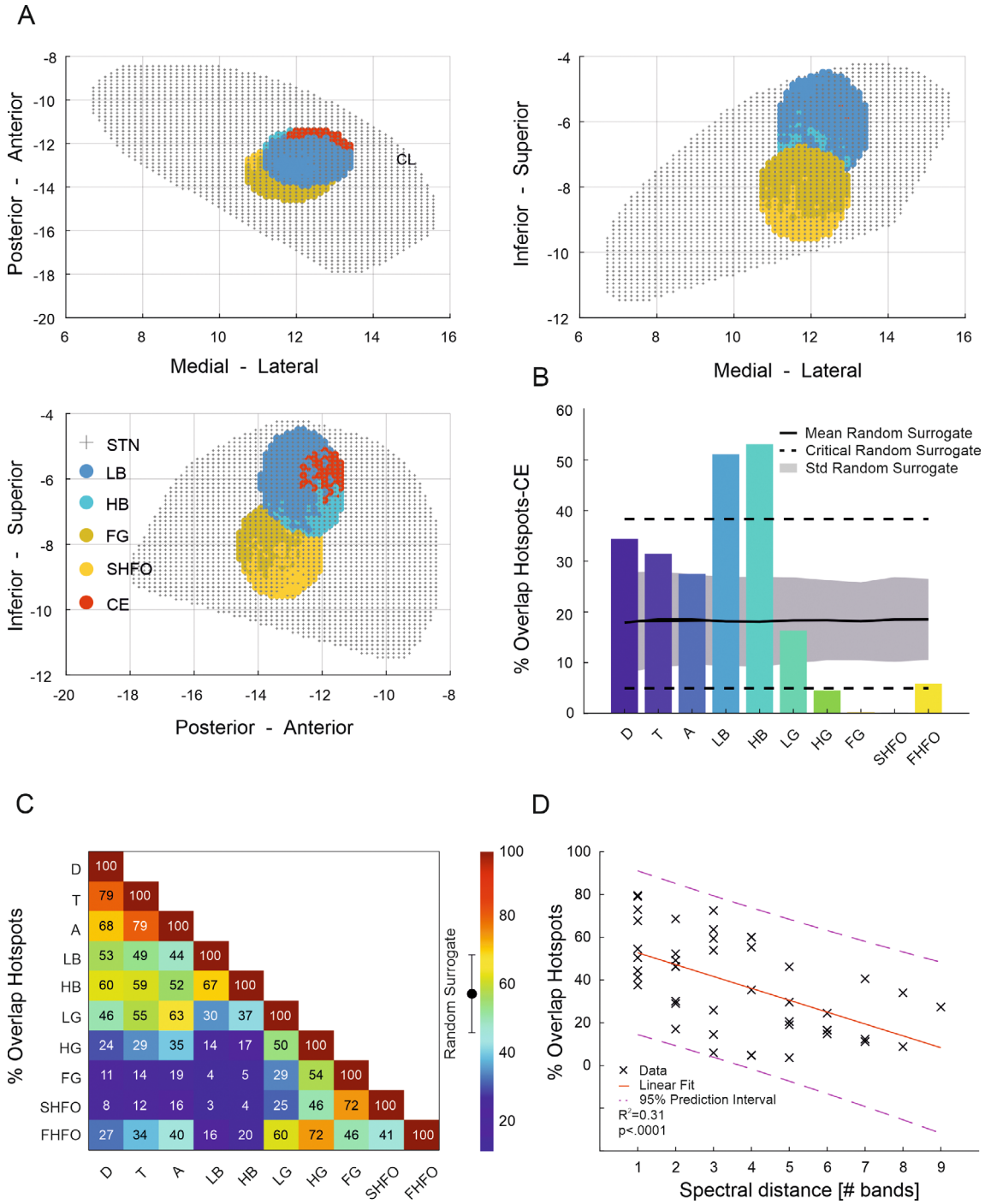

FIG. 4. Overlap (OVL) of clinical and spectral hot spots. (**A**) 2D probabilistic representation of a selection of representative spectral (ie, LB, HB, FG, and SHFO) and CE hot spots within the STN grid. In the top-right subplot depicting the inferior–superior and medial–lateral axes, the CE hot spot is covered by the spectral hot spots given its more posterior location. (**B**) Bar plot showing the percentage OVL between the spectral hot spot and clinical hot spot. Black line, shaded area, and dotted line represent the mean, SD (standard deviation), and critical values ($\alpha = [0.025, 0.975]$) of the random surrogate distribution. The LB and HB sub-bands share the largest volume with the clinical hot spot, and HG, FG, and SHFO share the lowest volume. (**C**) Color plot showing the percentage OVL between the spectral hot spots. Black dot indicates the mean level of OVL with the SD of the random surrogate distribution. (**D**) Linear regression (red line) with 95% confidence boundaries (dashed purple lines) calculated between spectral hot spots grouped according to 1/f (*x*-axis) and the percentage OVL (*y*-axis). Spectrally neighboring sub-bands show a higher spatial OVL. STN, subthalamic nuclei; D, delta; T, theta; A, alpha; LB, low-beta; HB, high-beta; LG, low-gamma; HG, high-gamma; FG, fast-gamma; SHFO, slow high-frequency oscillation; FHFO, fast high-frequency oscillation; CE, clinical efficacy. [Color figure can be viewed at wileyonlinelibrary.com]

(1.43) is the most focal compared to all other sub-bands (Fig. 3B).

Spectral–Clinical Topographic Map

To estimate the spatial relationship between the multiple spectral hot spots and the CE hot spot, we modeled the hot spot volumes and computed the percentage of spatial OVL between these regions (Fig. 4A). Both the LB (52.05%) and HB (52.93%) sub-bands shared the largest volume with the clinical hot spot (Fig. 4B). The opposite result was found for HG (4.62%), FG (0.05%), and SHFO (0%), which shared the significantly lowest amount of anatomical space with the clinical hot spot. Even when following a more conservative approach by including hemispheres with a minimum of two-point rigidity at baseline (instead of one), the results were similar (Fig. S3). The percentage OVL across the sub-bands was highest for spectrally neighboring bands (eg, 79% for alpha/theta) and lowest for spectrally distant bands (eg, 3% for LB/SHFO). The OVL across random surrogate hot spots was constant with a mean percentage OVL of 58.2% ± 13 (mean ± SD, Fig. 4C).

Spectral Topography to Predict the Clinical Response to DBS

Finally, we tested whether the spectral topographic map determined on a training data set is predictive for

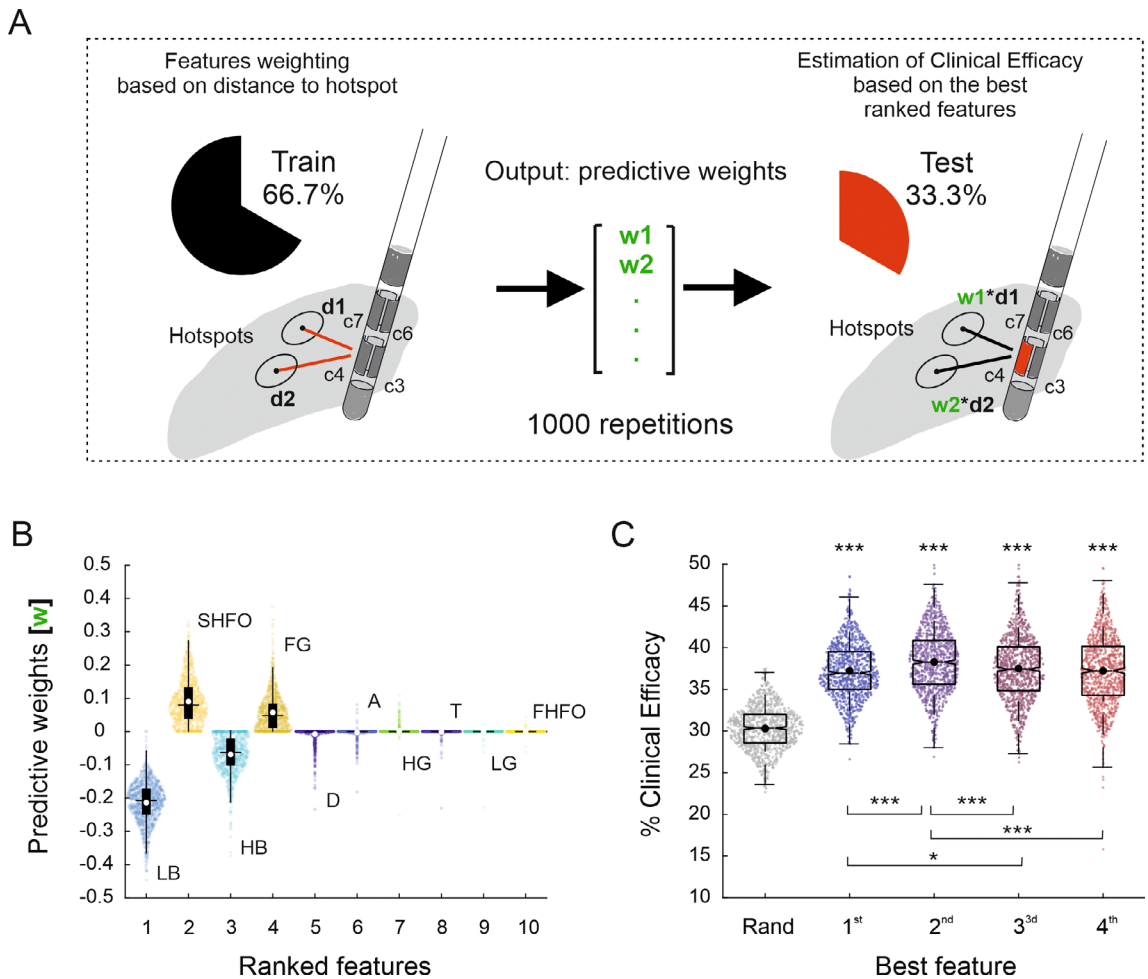

FIG. 5. STN (subthalamic nucleus) spectral topography and DBS outcome prediction. (**A**) Schematic summarizing the two-step contact prediction pipeline for the clinical response to DBS based on spectral topography. The predictive weights (w) of the features, determined as distances (d) of the stimulation contacts relative to the spectral hot spot centers of the 10 sub-bands, were calculated in the train data set. These were used on the test data set to predict the clinical response to DBS. (**B**) Predictive weights (w) derived from the train data set (66.6%) for the 10 predictor variables and ranked according to the predictive value from high to low. Each dot represents a single-fitted coefficient associated to the regression between the predictor variables and the outcome for the different iterations (n = 1000). The four most predictive features are LB (negative predictive weight), SHFO (negative predictive weight), HB (negative predictive weight), and FG (positive predictive weight). (**C**) Clinical efficacy predicted on the hold-out set (33.3%) by the algorithm and illustrated for the four best features. All the four best-ranked features significantly outperformed the prediction by chance. Significance levels against the random distribution are indicated on top, and significance levels of the comparison of the predictive value between features are indicated below the boxplots (*$P < 0.05$, **$P < 0.001$, and ***$P < 0.0001$); boxplots indicate the median, the 25th and 75th percentiles, and 1.5 interquartile range. d, distance; w, weight; DBS, deep brain stimulation; D, delta; T, theta; A, alpha; LB, low-beta; HB, high-beta; LG, low-gamma; HG, high-gamma; FG, fast-gamma; SHFO, slow high-frequency oscillation; FHFO, fast high-frequency oscillation; Rand, random surrogate distribution. [Color figure can be viewed at wileyonlinelibrary.com]

the DBS outcome of the naive test data set, with the prediction based on the distances of the contacts relative to the spectral hot spots (Fig. 5A). Using an elastic net regression model (Fig. S4), we first determined the predictive weight of the features (ie, distances to the hot spots for the 10 sub-bands) and ranked them according to their absolute predictive value from high to low (Fig. 5B). The four most predictive features for contacts with a high CE were LB (positive predictive weight), SHFO (negative predictive weight), HB (positive predictive weight), and FG (negative predictive weight). Finally, Figure 5C shows the predicted CE for the four highest-ranked features as follows: first: 37.2% ± 3.2; second: 38.3% ± 3.8; third: 37.5% ± 3.9; and fourth: 37.2% ± 4.2; all significantly outperformed the prediction by chance 30.3% ± 2.6 ($P < 0.001$).

Discussion

In this work, we present the spectral and clinical topography of the STN on a large cohort of PD patients implanted with multicontact DBS leads, thereby considering a wide range of spectral bands. We found that spectral features ranging from the delta-frequency band through HFOs are topographically segregated within the STN and may further differentiate in their spatial focality. The projection of both the spectral and clinical hot spots into the STN revealed a varying degree of spatial OVL, highest for the LB hot spot and lowest for the SHFO hot spot. Finally, the distance between the DBS-lead contacts and the spectral hot spots is predictive for the rigidity response to DBS, which supports the clinical utility of the spectral STN topography.

Spatial Segregation and Properties of Spectral Biomarkers

The functional topography of the STN is of major interest to guide advanced therapies such as DBS and highly focused ultrasound and to explain the clinical and behavioral characteristics of patients with PD. In fact, the present work shows that spectral LFP features may have a segregated location within the STN, which was most pronounced between the beta and FG/SHFO sub-bands. The inverse functional relationship between these two frequency bands is well described in the literature, with an anti-kinetic role attributed to beta and a prokinetic role attributed to gamma and higher frequencies.[14,37-39] Importantly, with the present findings we may provide an anatomical explanation for this inverse spectral–clinical relationship, as both sub-bands are spatially segregated within the STN. The beta hot spot is localized more superior in the motor STN relative to other spectral bands, thereby sharing the largest volume with the CE hot spot. The higher-frequency hot spots are localized more medial, inferior, and posterior to the beta hot spot. Although the anatomical positions of the LB and HB hot spots are comparable to previous work of comparable cohort size,[40] it is worth mentioning that the results of the topographic distribution across the different bands within the STN were not consistent with all previous reports. Some studies found the power of higher-frequency bands (eg, HG and HFO) recorded from both DBS electrodes and microelectrodes to be more prominent in the ventral STN.[24,27,41] Other studies located the higher frequencies more superior to the beta hot spot, toward the dorsal border of STN.[42,43] Such discrepancies may be attributed to multiple factors, such as the sample size, the resolution of the recording hardware (microelectrodes, segmented contacts, and ring contacts), and the recording montage (monopolar vs. bipolar). In particular, the use of DBS ring contacts with bipolar recording montage may not perfectly localize the source origin of neuronal oscillations[44] and be confounded by different spectral or connectivity properties.[45] The present work incorporates the so-far largest spectral range of features, extracted from monopolar signals recorded via multicontact DBS leads. And in fact, the low- to high-frequency spatial distribution of power found here was similar to Zaidel et al, a study conducted using high-resolution MER on a similarly large data set.[27]

But what is giving rise to such a spectral topographic map in the STN? As part of the basal ganglia cortical loop, the STN is functionally connected to different brain regions that require a specialized microarchitecture with distinct firing characteristic.[46-50] Moreover, subregions with specific frequency distributions and somatotopic and functional representations (motor, associative, and limbic) can be delineated at the cortical level,[51-53] which to a varying degree are also preserved throughout the cortical–subcortical loops.[54-60] The intrinsic organization of the brain combining neuronal segregation and integration within and across different networks facilitates adaptive control and may ultimately give rise to such differentiated spectral-spatial brain characteristics.[61,62] In addition to the spatial segregation of hot spots, the different sub-bands differentiate in other spatial properties such as their degrees of focality. Here we found that beta activity was spatially more spread in comparison to all other spectral features. This may be because beta activity is a prevalent spectral feature related to motor processing with a dominant presence in the motor part of the STN.[63] However, the more spread distribution could also be the consequence of the dopaminergic deficiency attributed to PD.[64] In fact, it remains to be seen whether spatial spread of local and long-range beta synchronization[65,66] expands with disease progression and whether this follows any specific anatomical pattern. In contrast, higher-frequency bands, such as FG and HFO, were spatially more circumscribed and may represent more organized interactions of a local

ensemble within STN.[24,67,68] The temporal interaction between frequency bands, which is well established for the phase amplitude coupling between beta oscillations and the HFOs,[18,23,69,70] could further be elaborated across spectra and with regard to their topographic properties.

Toward Automatization of DBS Programming

One clinical application of brain sense technology is to inform DBS programming.[3-5,71] Our spectral topography–based DBS response prediction confirms the utility of STN beta activity to identify the optimal stimulation site to improve rigidity or bradykinesia as indexed by other studies.[3-5,27,72-74] Although recent publications suggested HB activity to be more predictive for optimal stimulation contact,[40,75] we found that LB activity still outperformed HB activity with regard to rigidity improvement, whereas both features were part of the four most predictive ones. The more inferiorly localized high-frequency features, particularly SHFO activity, have a strong negative predictive power for the rigidity based–DBS outcome, which is in line with previous data.[4,76] Thus, according to the present results, we may assume that DBS programming for controlling motor impairment, presently indexed as the level of rigidity, could rely on both beta oscillations and SHFOs. Moreover, it needs to be considered that the implementation of brain-sensing is not top priority for all different neurostimulator manufacturers and it may be limited by signal artifacts or other technical causes in individual subjects.[77,78] For these scenarios, a spectral topographic map may still be informative as a reference atlas tool to inform multicontact DBS programming, alone or in conjunction with imaging, modeling, or wearable tools.[4,6,32,79,80]

Impact on aDBS

What does the spectral topographic distribution imply for the design of aDBS? The feedback signal that drives aDBS should have the best-possible signal-to-noise ratio to trigger stimulation accurately.[77] Therefore, the optimal montage of the recording contacts relative to the signal source is one important determinant. Although aDBS control policies based on beta activity are closest to clinical implementation,[2,7] future aDBS algorithms may be improved by incorporating other neurophysiological markers with potentially distinct spatial and temporal properties.[8,81,82] Considering the 2 mm group-level distance found between the beta and FG hot spots would imply that the optimal aDBS recording setup for controlling hypokinetic symptoms (eg, beta-frequency range) might be different from tremor/dyskinesia control (higher-frequency range). In addition, both low- and high-frequency features can be inversely and accurately indicative of the control of the same symptom, and such bivalent clinical–spectral relationship could be advantageous for future aDBS control algorithms. Moreover, the versatility of the stimulation-recording configuration at the level of the subcortical DBS target structure is limited, and future alternative setups may include cortical sensing combined with subcortical stimulation in line with the functional topography of the STN.[83,84]

Limitations

The topographic distribution presented in this work primarily covers the more dorsal part of the STN, which corresponds to the surgical target region for DBS in PD. The clinical assessment during the monopolar contact review is limited to upper-limb rigidity assessment, which is considered the most sensitive clinical sign for the monopolar contact review.[34] Testing the multicontact DBS response for a broad range of clinical symptoms would not have been practically feasible. However, the spectral and clinical topography of other motor and non-motor symptoms may follow a distinct pattern[58,85] and require dedicated studies. Furthermore, the spectral topography was established for the *off* dopaminergic and resting state; however, it is possible that spatial properties might change depending on the medication and activity states. The exact definitions of the frequency boundaries are somehow arbitrary and may slightly vary in comparison to previous literature. Future spectral topographic investigations could focus on the individually most informative frequency components that could be detected using methods such as hidden Markov modeling.[86] Because the LFPs were recorded intraoperatively after the MER was performed, we cannot exclude some reduction in the signal-to-noise ratio due the lesion effect.[87] Furthermore, minor deviations in lead orientation after lead insertion could have affected the accuracy of the topographic distribution in the horizontal plane.[33] Finally, anatomical group analyses were possible only after spatial normalization and projection of contact coordinates into the MNI space, which may have introduced some distortion of the lead–STN anatomical relationship in some hemispheres.

Conclusions and Outlook

In conclusion, with the present work we complement the spectral biomarker landscape with the corresponding spatial properties within the STN and demonstrate that this spectral topography of the STN can inform about the response to DBS. This adds to a better understanding of the functional and spectral architecture of the STN and may inspire future clinical–anatomical mapping studies using DBS or high-intensity-focused ultrasound to provide an even-finer

granularity for such multimodal maps.[58] The spectral topography of the STN may serve as a tool to guide patient-tailored intervention such as advanced multicontact programming and next-generation sensing-based DBS. ■

Acknowledgments: G.T., E.B., and A.A. received funding from the Swiss National Science Foundation (project number: PZ00P3_202166). T. A.K.N. also received funding from the Swiss National Science Foundation. B.D. was supported by the Medical Research Council (grant number: 186142 MC_UU_00003/1). Open access funding provided by Inselspital Universitatsspital Bern.

Conflict of Interest

GT received financial support from Boston Scientific and Medtronic not related to the present work. Research agreement with RuneLabs not related to the present work. AN received consulting fees from Medtronic not related to this work. M.L.L. received reimbursement of traveling expenses to scientific meetings by Medtronic, Teva Pharmaceutical Industries, Zambon and BIAL.

Data Availability Statement

The data that support the findings of this study are available from the corresponding author upon reasonable request.

References

1. Krack P, Volkmann J, Tinkhauser G, Deuschl G. Deep brain stimulation in movement disorders: from experimental surgery to evidence-based therapy. Mov Disord 2019;34:1795–1810.
2. Meidahl AC, Tinkhauser G, Herz DM, Cagnan H, Debarros J, Brown P. Adaptive deep brain stimulation for movement disorders: the long road to clinical therapy. Mov Disord 2017;32:810–819.
3. Tinkhauser G, Pogosyan A, Debove I, et al. Directional local field potentials: a tool to optimize deep brain stimulation. Mov Disord 2018;33:159–164.
4. Shah A, Nguyen TAK, Peterman K, et al. Combining multimodal biomarkers to guide deep brain stimulation programming in Parkinson disease. Neuromodulation 2022;26(2):320–332.
5. Milosevic L, Scherer M, Cebi I, et al. Online mapping with the deep brain stimulation Lead: a novel targeting tool in Parkinson's disease. Mov Disord 2020;35:1574–1586.
6. di Biase L, Tinkhauser G, Martin Moraud E, Caminiti ML, Pecoraro PM, Di Lazzaro V. Adaptive, personalized closed-loop therapy for Parkinson's disease: biochemical, neurophysiological, and wearable sensing systems. Expert Rev Neurother 2021;21:1371–1388.
7. Little S, Brown P. Debugging adaptive deep brain stimulation for Parkinson's disease. Mov Disord 2020;35:555–561.
8. Tinkhauser G, Moraud EM. Controlling clinical states governed by different temporal dynamics with closed-loop deep brain stimulation: a principled framework. Front Neurosci 2021;15:734186.
9. Brown P, Oliviero A, Mazzone P, Insola A, Tonali P, Di Lazzaro V. Dopamine dependency of oscillations between subthalamic nucleus and pallidum in Parkinson's disease. J Neurosci 2001;21:1033–1038.
10. Kühn AA, Kupsch A, Schneider GH, Brown P. Reduction in subthalamic 8–35 Hz oscillatory activity correlates with clinical improvement in Parkinson's disease. Eur J Neurosci 2006;23:1956–1960.
11. Tinkhauser G, Pogosyan A, Tan H, Herz DM, Kühn AA, Brown P. Beta burst dynamics in Parkinson's disease OFF and ON dopaminergic medication. Brain 2017;140:2968–2981.
12. Neumann WJ, Turner RS, Blankertz B, Mitchell T, Kühn AA, Richardson RM. Toward electrophysiology-based intelligent adaptive deep brain stimulation for movement disorders. Neurotherapeutics 2019;16:105–118.
13. van Wijk BCM, de Bie RMA, Beudel M. A systematic review of local field potential physiomarkers in Parkinson's disease: from clinical correlations to adaptive deep brain stimulation algorithms. J Neurol 2022;2022(1):1–16.
14. Fogelson N, Pogosyan A, Kühn AA, et al. Reciprocal interactions between oscillatory activities of different frequencies in the subthalamic region of patients with Parkinson's disease. Eur J Neurosci 2005;22:257–266.
15. Wiest C, Torrecillos F, Tinkhauser G, et al. Finely-tuned gamma oscillations: spectral characteristics and links to dyskinesia. Exp Neurol 2022;351:113999.
16. Swann NC, De Hemptinne C, Miocinovic S, et al. Gamma oscillations in the hyperkinetic state detected with chronic human brain recordings in Parkinson's disease. J Neurosci 2016;36(24):6445–6458.
17. Hirschmann J, Butz M, Hartmann CJ, et al. Parkinsonian rest tremor is associated with modulations of subthalamic high-frequency oscillations. Mov Disord 2016;31:1551–1559.
18. López-Azcárate J, Tainta M, Rodríguez-Oroz MC, et al. Coupling between Beta and High-frequency activity in the human subthalamic nucleus may Be a pathophysiological mechanism in Parkinson's disease. J Neurosci 2010;30:6667–6677.
19. Ozturk M, Abosch A, Francis D, Wu J, Jimenez-Shahed J, Ince NF. Distinct subthalamic coupling in the ON state describes motor performance in Parkinson's disease. Mov Disord 2020;35:91–100.
20. Rappel P, Grosberg S, Arkadir D, et al. Theta-alpha oscillations characterize emotional subregion in the human ventral subthalamic nucleus. Mov Disord 2020;35:337–343.
21. Huebl J, Schoenecker T, Siegert S, et al. Modulation of subthalamic alpha activity to emotional stimuli correlates with depressive symptoms in Parkinson's disease1. Mov Disord 2011;26:477–483.
22. Ricciardi L, Fischer P, Mostofi A, et al. Neurophysiological correlates of trait impulsivity in Parkinson's disease. Mov Disord 2021;36:2126–2135.
23. van Wijk BCM, Beudel M, Jha A, et al. Subthalamic nucleus phase–amplitude coupling correlates with motor impairment in Parkinson's disease. Clin Neurophysiol 2016;127:2010–2019.
24. Wang J, Hirschmann J, Elben S, et al. High-frequency oscillations in Parkinson's disease: spatial distribution and clinical relevance. Mov Disord 2014;29:1265–1272.
25. Lourens MAJ, Meijer HGE, Contarino MF, et al. Functional neuronal activity and connectivity within the subthalamic nucleus in Parkinson's disease. Clin Neurophysiol 2013;124:967–981.
26. Verhagen R, Zwartjes DGM, Heida T, et al. Advanced target identification in STN-DBS with beta power of combined local field potentials and spiking activity. J Neurosci Methods 2015;253:116–125.
27. Zaidel A, Spivak A, Grieb B, Bergman H, Israel Z. Subthalamic span of β oscillations predicts deep brain stimulation efficacy for patients with Parkinson's disease. Brain 2010;133:2007–2021.
28. Horn A, Neumann WJ, Degen K, Schneider GH, Kühn AA. Toward an electrophysiological "sweet spot" for deep brain stimulation in the subthalamic nucleus. Hum Brain Mapp 2017;38:3377–3390.
29. Foffani G, Priori A, Egidi M, et al. 300-Hz subthalamic oscillations in Parkinson's disease. Brain 2003;126:2153–2163.
30. Horn A, Kühn AA. Lead-DBS: a toolbox for deep brain stimulation electrode localizations and visualizations. Neuroimage 2015;107:127–135.
31. Avants BB, Epstein CL, Grossman M, Gee JC. Symmetric diffeomorphic image registration with cross-correlation: evaluating automated labeling of elderly and neurodegenerative brain. Med Image Anal 2008;12:26–41.

32. Ewert S, Plettig P, Li N, et al. Toward defining deep brain stimulation targets in MNI space: a subcortical atlas based on multimodal MRI, histology and structural connectivity. Neuroimage 2018;170: 271–282.
33. Lange F, Steigerwald F, Engel D, et al. Longitudinal assessment of rotation angles after implantation of directional deep brain stimulation leads. Stereotact Funct Neurosurg 2021;99:150–158.
34. Volkmann J, Moro E, Pahwa R. Basic algorithms for the programming of deep brain stimulation in Parkinson's disease. Mov Disord 2006;21:S284–S289.
35. Silverman BW. *Density estimation for statistics and data analysis*. Vol. 26. Boca Raton, FL: CRC press, 1986.
36. Zou H, Hastie T. Regularization and variable selection via the elastic net. J R Stat Soc Ser B: Stat Methodol 2005;67:301–320.
37. Litvak V, Eusebio A, Jha A, et al. Movement-related changes in local and long-range synchronization in parkinson's disease revealed by simultaneous magnetoencephalography and intracranial recordings. J Neurosci 2012;32:10541–10553.
38. Cassidy M, Mazzone P, Oliviero A, et al. Movement-related changes in synchronization in the human basal ganglia. Brain 2002;125: 1235–1246.
39. Brown P. Oscillatory nature of human basal ganglia activity: relationship to the pathophysiology of Parkinson's disease. Mov Disord 2003;18:357–363.
40. Darcy N, Lofredi R, Al-Fatly B, et al. Spectral and spatial distribution of subthalamic beta peak activity in Parkinson's disease patients. Exp Neurol 2022;356:114150.
41. Özkurt TE, Butz M, Homburger M, et al. High frequency oscillations in the subthalamic nucleus: a neurophysiological marker of the motor state in Parkinson's disease. Exp Neurol 2011;229:324–331.
42. van Wijk BCM, Pogosyan A, Hariz MI, et al. Localization of beta and high-frequency oscillations within the subthalamic nucleus region. NeuroImage Clin 2017;16:175–183.
43. Geng X, Xu X, Horn A, et al. Intra-operative characterisation of subthalamic oscillations in Parkinson's disease. Clin Neurophysiol 2018;129:1001–1010.
44. Maling N, Lempka SF, Blumenfeld Z, Bronte-Stewart H, McIntyre CC. Biophysical basis of subthalamic local field potentials recorded from deep brain stimulation electrodes. J Neurophysiol 2018;120:1932–1944.
45. Averna A, Marceglia S, Arlotti M, et al. Influence of inter-electrode distance on subthalamic nucleus local field potential recordings in Parkinson's disease. Clin Neurophysiol 2022;133:29–38.
46. Rodriguez-Oroz MC, Rodriguez M, Guridi J, et al. The subthalamic nucleus in Parkinson's disease: somatotopic organization and physiological characteristics. Brain 2001;124:1777–1790.
47. Weinberger M, Mahant N, Hutchison WD, et al. Beta oscillatory activity in the subthalamic nucleus and its relation to dopaminergic response in Parkinson's disease. J Neurophysiol 2006;96:3248–3256.
48. Kaku H, Ozturk M, Viswanathan A, et al. Unsupervised clustering reveals spatially varying single neuronal firing patterns in the subthalamic nucleus of patients with Parkinson's disease. Clin Parkinsonism Relat Disord 2020;3:100032.
49. Mosher CP, Mamelak AN, Malekmohammadi M, Pouratian N, Rutishauser U. Distinct roles of dorsal and ventral subthalamic neurons in action selection and cancellation. Neuron 2021;109:869–881.e6.
50. Milosevic L, Kalia SK, Hodaie M, et al. A theoretical framework for the site-specific and frequency-dependent neuronal effects of deep brain stimulation. Brain Stimul 2021;14:807–821.
51. Frauscher B, Von Ellenrieder N, Zelmann R, et al. Atlas of the normal intracranial electroencephalogram: neurophysiological awake activity in different cortical areas. Brain 2018;141:1130–1144.
52. Keitel A, Gross J. Individual human brain areas can Be identified from their characteristic spectral activation fingerprints. PLoS Biol 2016;14:e1002498.
53. Capilla A, Arana L, García-Huéscar M, Melcón M, Gross J, Campo P. The natural frequencies of the resting human brain: an MEG-based atlas. Neuroimage 2022;258:119373.
54. Nambu A, Takada M, Inase M, Tokuno H. Dual somatotopical representations in the primate subthalamic nucleus: evidence for ordered but reversed body-map transformations from the primary motor cortex and the supplementary motor area. J Neurosci 1996;16:2671–2683.
55. Iwamuro H, Tachibana Y, Ugawa Y, Saito N, Nambu A. Information processing from the motor cortices to the subthalamic nucleus and globus pallidus and their somatotopic organizations revealed electrophysiologically in monkeys. Eur J Neurosci 2017;46:2684–2701.
56. Krack P, Kumar R, Ardouin C, et al. Mirthful laughter induced by subthalamic nucleus stimulation. Mov Disord 2001;16:867–875.
57. Accolla EA, Herrojo Ruiz M, Horn A, et al. Brain networks modulated by subthalamic nucleus deep brain stimulation. Brain 2016; 139:2503–2515.
58. Rodriguez-Rojas R, Pineda-Pardo JA, Mañez-Miro J, et al. Functional topography of the human subthalamic nucleus: relevance for subthalamotomy in Parkinson's disease. Mov Disord 2021;37(2): 279–290.
59. Tinkhauser G, Shah AS, Fischer P, et al. Electrophysiological differences between upper and lower limb movements in the human subthalamic nucleus. Clin Neurophysiol 2019;130:727–738.
60. Averna A, Arlotti M, Rosa M, et al. Pallidal and cortical oscillations in freely moving patients with dystonia. Neuromodulation: journal of the International Neuromodulation Society 2021.
61. Tononi G, Sporns O, Edelman GM. A measure for brain complexity: relating functional segregation and integration in the nervous system. Proc Natl Acad Sci 1994;91:5033–5037.
62. Mohr H, Wolfensteller U, Betzel RF, et al. Integration and segregation of large-scale brain networks during short-term task automatization. Nat Commun 2016;7(1):1–12.
63. Engel AK, Fries P. Beta-band oscillations — signalling the status quo? Curr Opin Neurobiol 2010;20:156–165.
64. Levy R, Dostrovsky JO, Lang AE, Sime E, Hutchison WD, Lozano AM. Effects of apomorphine on subthalamic nucleus and globus pallidus internus neurons in patients with Parkinson's disease. J Neurophysiol 2001;86:249–260.
65. Tinkhauser G, Torrecillos F, Duclos Y, et al. Beta burst coupling across the motor circuit in Parkinson's disease. Neurobiol Dis 2018; 117:217–225.
66. Oswal A, Cao C, Yeh CH, et al. Neural signatures of hyperdirect pathway activity in Parkinson's disease. Nat Commun 2021;12: 1–14.
67. Telkes I, Viswanathan A, Jimenez-Shahed J, et al. Local field potentials of subthalamic nucleus contain electrophysiological footprints of motor subtypes of Parkinson's disease. Proc Natl Acad Sci U S A 2018;115:E8567–E8576.
68. Bragin A, Wilson CL, Engel J. Chronic epileptogenesis requires development of a network of pathologically interconnected neuron clusters: a hypothesis. Epilepsia 2000;41:S144–S152.
69. De Hemptinne C, Ryapolova-Webb ES, Air EL, et al. Exaggerated phase-amplitude coupling in the primary motor cortex in Parkinson disease. Proc Natl Acad Sci U S A 2013;110:4780–4785.
70. Meidahl AC, Moll CKE, van Wijk BCM, et al. Synchronised spiking activity underlies phase amplitude coupling in the subthalamic nucleus of Parkinson's disease patients. Neurobiol Dis 2019;127: 101–113.
71. Telkes I, Sabourin S, Durphy J, et al. Functional use of directional local field potentials in the subthalamic nucleus deep brain stimulation. Front Hum Neurosci 2020;14:145.
72. Yoshida F, Martinez-Torres I, Pogosyan A, et al. Value of subthalamic nucleus local field potentials recordings in predicting stimulation parameters for deep brain stimulation in Parkinson's disease. J Neurol Neurosurg Psychiatry 2010;81:885–889.
73. Bour LJ, Lourens MAJ, Verhagen R, et al. Directional recording of subthalamic spectral power densities in Parkinson's disease and the effect of steering deep brain stimulation. Brain Stimul 2015;8: 730–741.
74. Nguyen TAK, Schüpbach M, Mercanzini A, Dransart A, Pollo C. Directional local field potentials in the subthalamic nucleus during deep brain implantation of Parkinson's disease patients. Front Hum Neurosci 2020;14:425.

75. Chen PL, Chen YC, Tu PH, et al. Subthalamic high-beta oscillation informs the outcome of deep brain stimulation in patients with Parkinson's disease. Front Hum Neurosci 2022;16:958521.

76. Hirschmann J, Steina A, Vesper J, Florin E, Schnitzler A. Neuronal oscillations predict deep brain stimulation outcome in Parkinson's disease. Brain Stimul 2022;15:792–802.

77. Ansó J, Benjaber M, Parks B, et al. Concurrent stimulation and sensing in bi-directional brain interfaces: a multi-site translational experience. J Neural Eng 2022;19:026025.

78. Neumann WJ, Memarian Sorkhabi M, Benjaber M, et al. The sensitivity of ECG contamination to surgical implantation site in brain computer interfaces. Brain Stimul 2021;14:1301–1306.

79. Jaradat A, Nowacki A, Montalbetti M, et al. Probabilistic subthalamic nucleus stimulation sweet spot integration into a commercial deep brain stimulation programming software can predict effective stimulation parameters. Neuromodulation 2023;26(2):348–355.

80. Nguyen TAK, Nowacki A, Debove I, et al. Directional stimulation of subthalamic nucleus sweet spot predicts clinical efficacy: proof of concept. Brain Stimul 2019;12:1127–1134.

81. Gilron R, Little S, Perrone R, et al. Long-term wireless streaming of neural recordings for circuit discovery and adaptive stimulation in individuals with Parkinson's disease. Nat Biotechnol 2021;39(9):1078–1085.

82. Averna A, Marceglia S, Priori A, Foffani G. Amplitude and frequency modulation of subthalamic beta oscillations jointly encode the dopaminergic state in Parkinson's disease. npj Parkinson's Dis 2022;8:131.

83. Swann NC, De Hemptinne C, Thompson MC, et al. Adaptive deep brain stimulation for Parkinson's disease using motor cortex sensing. J Neural Eng 2018;15:046006.

84. Zamora M, Toth R, Morgante F, et al. DyNeuMo Mk-1: design and pilot validation of an investigational motion-adaptive neurostimulator with integrated chronotherapy. Exp Neurol 2022;351:113977.

85. Akram H, Georgiev D, Mahlknecht P, et al. Subthalamic deep brain stimulation sweet spots and hyperdirect cortical connectivity in Parkinson's disease. Neuroimage 2017;158:332–345.

86. Khawaldeh S, Tinkhauser G, Torrecillos F, et al. Balance between competing spectral states in subthalamic nucleus is linked to motor impairment in Parkinson's disease. Brain 2022;145:237–250.

87. Chen CC, Pogosyan A, Zrinzo LU, et al. Intra-operative recordings of local field potentials can help localize the subthalamic nucleus in Parkinson's disease surgery. Exp Neurol 2006;198:214–221.

Supporting Data

Additional Supporting Information may be found in the online version of this article at the publisher's web-site.

SGML and CITI Use Only
DO NOT PRINT

Author Roles

(1) Research project: A. Conception, B. Organization, C. Execution; D. Data collection; (2) Statistical analysis: A. Design, B. Execution, C. Review and critique; (3) Manuscript preparation: A. Writing of the first draft, B. Review and critique.

A.A.: 1A, 1B, 1C, 2A, 2B, 3A, 3B
I.D.: 1D, 3B
A.N.: 1D, 3B
K.P.: 1D, 2C, 3B
B.D: 2C, 3B
M.S.: 2C, 3B
E.B.: 2C, 3B
L.A.: 2C, 3B
M.L.L.: 1D, 3B
M.S.: 1D, 3B
C.P.: 1D, 3B
P.K.: 1D, 3B
T.A.K.N.: 1D, 2C, 3B
G.T.: 1A, 1B, 1D, 2A, 2C, 3A, 3B